Elsevier Editorial System(tm) for Applied Surface Science

Manuscript Draft

Manuscript Number: APSUSC-D-18-00041R1

Title: Asymmetrical Bonding in Cold Spraying of Dissimilar Materials

Article Type: Full Length Article

Keywords: Cold spray, Dissimilar bonding, Finite element modelling, Deformation enhanced interdiffusion, NiTi intermetallic.

Corresponding Author: Professor Hamid Assadi,

Corresponding Author's Institution: Brunel University London

First Author: Roghayeh Nikbakht

Order of Authors: Roghayeh Nikbakht; Seyed Hossein Seyedein, PhD, Professor; Shahram Kheirandish, PhD, Professor; Hamid Assadi, PhD, Professor; Bertrand Jodoin, PhD, Professor

Cover Letter

Dear Prof. Montemor,

We have carefully reviewed the comments and have revised the manuscript accordingly. Changes to the manuscript are shown highlighted in the revised manuscript. I would very much appreciate, if you could consider the revised manuscript for publication in Applied Surface Science.

Kind regards,

Hamid Assadi

***Highlights (for review)**

Cold spraying experiments of asymmetrical Ni/Ti and Ti/Ni (particle/substrate) pairs were performed to study deformation and bonding phenomena.

Impact morphology and deformation of single splats were modelled through FEM simulations using PTW plasticity model to account for large strain rates.

Annealing experiments and consequently formed interfacial intermetallics layer were investigated.

Correlation of interfacial intermetallics pattern with highly strained interface area, predicted by modelling, present a new insight to the extent of particle/substrate metallurgical bonding.

Metallurgical bonding of a particle/substrate is more likely to be found at peripheral areas of the interface which extends from there to the base of the particle with increase of kinetic energy of impacting particle.

Graphical Abstract (for review)

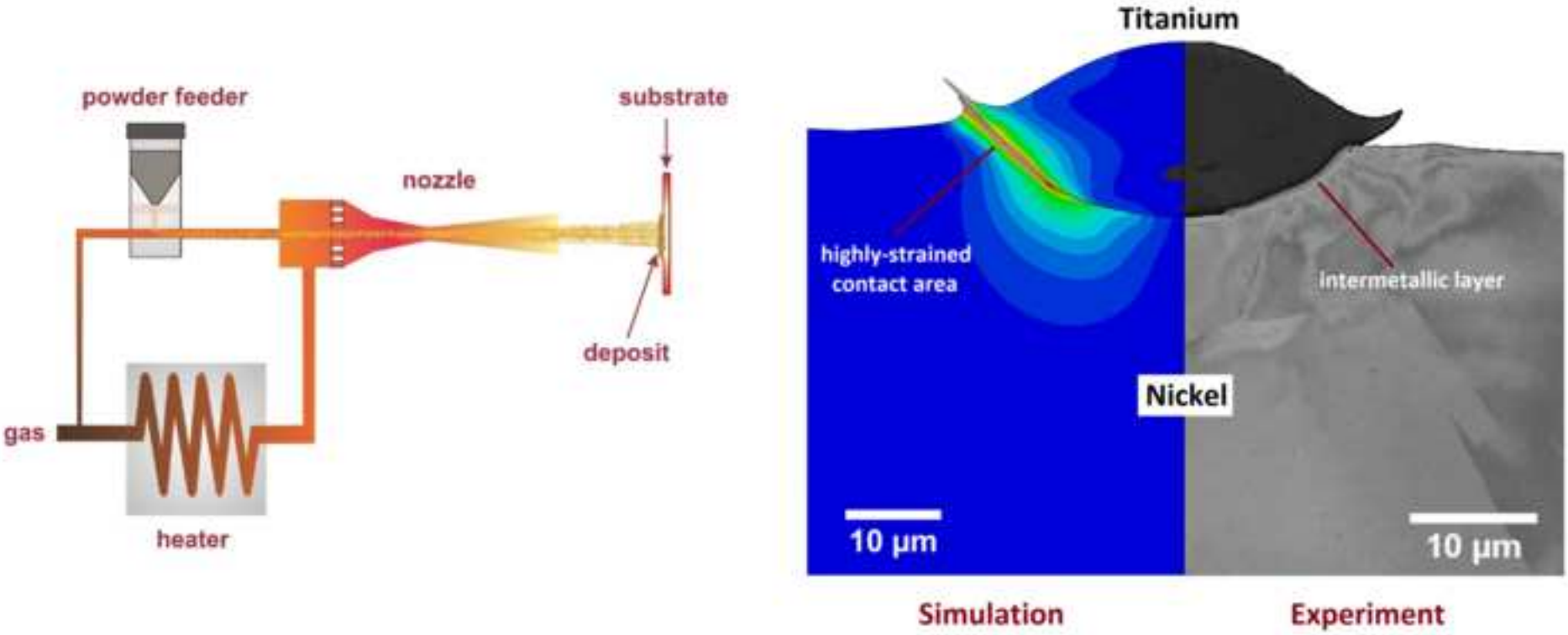

Response to Reviewer 1:

Thank you for your review of our paper.

1. Abstract: Characterisation of the as-sprayed samples reveal that for the Ni(particle)/Ti(substrate) pair, plastic deformation of the particle is dominating whereas for the Ti(particle)/Ni(substrate) pair the substrate and particle deform to similar extents." The sentence is difficult to read, please rewrite. In general, the authors use too long sentences, the reading will be improved once shorter sentences are employed.

Response: The long sentence was edited as follows: Characterisation of the as-sprayed samples reveal that for the Ni(particle)/Ti(substrate) pair, plastic deformation of the particle is dominating over substrate deformation. However, for the Ti(particle)/Ni(substrate) pair, it is observed that the substrate and particle deform to similar extents. (p. 2, lines 1–4).

2. Experimental procedure: Please specify how the powders were produced. It is useful to indicate the hardness of the starting substrates and (if it is possible) the hardness of the powders (probably known from the suppliers).

Response: Both powders are mostly spherical and produced by a gas atomization method. (p.6, line 8). The Vickers micro-hardness ($HV_{0.025}$) of Ni and Ti substrates respectively were 117 and 171. (p. 6, line 11-12). Powder hardness can also be obtained but we don't have nano-hardness so micro-hardness was measured although not as accurate.

3. Numerical modelling. Please delete "commonly used in CS modelling" in line 3.

Response: It was deleted. (p. 7, the last line)

4. What about particles and substrates mechanical properties? Are taken into account in the simulations or not?

Response: Yes these are taken into account by the model and the following sentence was added to the manuscript: The mechanical properties including saturation stress, yield stress, strain (rate)

hardening constant and coefficient are defined in equations 4 to 8. The values of mechanical properties are given in Table 4. (p. 11, lines 6-7)

5. Results and discussion, Particles seem to exhibit different splat rates. How the authors choose those to be compared with the FEM simulations? This is a crucial point for the understanding of the paper results.

Response: We chose the splat shapes that were the most frequently observed and the following explanations have been added to the clarity of the point: Results and discussions: Besides, the impact morphologies of N_2 and He-sprayed Ti splats show that He gas as a process gas provides a broader range of impact velocities [52]. (p. 14, lines 2-4)

The most frequently observed impact morphologies were taken to represent the impact conditions of the corresponding particle size. In the case of Ti/Ni pairs, for instance, large Ti splats with low flattening ratio were observed for both cases of spraying with He and N_2. However, this morphology was significantly more frequently observed in N_2-sprayed samples – hence taken as representing the impact conditions of large Ti particles only for the case of spraying with N_2. The most frequently observed splat morphologies for Ti/Ni and Ni/Ti pairs – which are to be compared to the corresponding modelled splats – are presented in Fig.7 (a3) (c3) and (d3). (p.18. lines 10-17)

*Manuscript
Click here to view linked References

Asymmetrical Bonding in Cold Spraying of Dissimilar Materials

R. Nikbakht [a], S.H. Seyedein [a], S. Kheirandish [b], H. Assadi [c,*], B. Jodoin [d]

[a] Iran University of Science and Technology, Materials Processing Simulation Laboratory (MPS – Lab), School of Materials and Metallurgical Engineering, Narmak, Tehran, Iran

[b] Iran University of Science and Technology, School of Metallurgy and Materials Engineering, Narmak, Tehran, Iran

[c] Brunel University London, Brunel Centre for Advanced Solidification Technology (BCAST), Uxbridge, United Kingdom

[d] University of Ottawa, 770 King Edward, Ottawa, ON, Canada K1N 6N5

* E-mail: hamid.assadi@brunel.ac.uk

Abstract

Characteristics of particle bonding, especially for dissimilar materials, remains a key question in cold spray deposition. There are limited reports in direct correlation to particle/substrate bonding and peripheral shear zones. Cold spraying experiments and numerical simulations are conducted to characterise and analyse the correlation between bonding and peripheral shear zones for asymmetric particle/substrate pairs of intermetallic-forming elements of nickel and titanium. The correlation between metallic bonding and highly strained areas is explored in view of the growth of the intermetallic phase at the particle/substrate interface during subsequent heat treatments.

Characterisation of the as-sprayed samples reveal that for the Ni(particle)/Ti(substrate) pair, plastic deformation of the particle is dominating over substrate deformation. However, for the Ti(particle)/Ni(substrate) pair, it is observed that the substrate and particle deform to similar extents. Characterisation of the samples after a brief heat treatment at 700°C indicate that intermetallic formation, and hence metallurgical bonding of the pairs is more likely to occur at the particle peripheries where the interface areas are highly strained, and rarely achieved at the particle base. Results also reveal that bonding extends from peripheries toward the central part of the interfaces with increasing the impact velocity.

The kinetics of interfacial intermetallic formation at peripheral areas and its correlation to particle bonding is discussed in view of deformation-enhanced interdiffusion.

Keywords: Cold spray, Dissimilar Bonding, Finite Element Modelling, Deformation Enhanced Interdiffusion, NiTi intermetallic.

1.Introduction

Cold Spray (CS) is a solid-state coating process where feedstock particles are accelerated to high speeds (300-1200 m/s) towards a substrate while maintaining temperatures well below their melting temperatures [1]. Owing to the low-temperature operation and inert gas shielding during the deposition process, CS is used for spraying temperature sensitive materials such as nanocrystalline materials [2, 3], alloys [4-7], energetic composite materials [8-11], polymers [12-14] and oxidation-sensitive material such as aluminum [15-17], titanium [18, 19], copper [16, 20], and magnesium [21, 22].

The kinetic energy of the accelerated particles causes intense plastic deformation (of both the particles and substrate) and mostly dissipates as heat [23-25]. Because of the high strain rates experienced by the particles (from 10^3 to 10^9 s^{-1}), there is little time for the diffusion of the generated heat [26], resulting in local thermal softening of the material that overcomes strain (and strain-rate) hardening effects [27]. This intensifies the localized particle plastic deformation up to the point where material shearing resistance breaks down leading to adiabatic shear instabilities (ASI) [25, 26]. ASI leads to material flowing outwards of the particle/substrate or particle/particle contact zone and disruption of native thin surface oxide films [1, 28, 29]. The subsequent clean and intimate contact of the materials combined with the existing localized high pressure as a result of impact promotes metallurgical bonding [26, 30].

Finite element modelling (FEM) has been extensively used for enhanced understanding of deformation and bonding mechanisms in CS. Different dynamic hardening models have been used to compute the flow stress of high strain rate deformations such as Johnson-Cook (JC) [8, 23, 25, 31-34], Preston–Tonks–Wallace (PTW) [15, 35, 36], Khan-Huang-Liang

(KHL) [35] and Zerilli and Armstrong (ZA) [35]. A comparative study on the simulation of single copper particle impact on copper substrates found that the PTW model predicted the deformation fairly accurately [35]. In addition, the PTW model has been successfully used for simulation of single impact deformation of materials such as aluminium [15], stainless steel (SS) 304 and nickel [36] in CS process. Bonding has been attributed to the thermal softening of the local area and intensified plastic deformation occurring at impact velocities around or beyond the critical velocity of the material [25, 26]. The local temperature increase and plastic strain were used as an indication of ASI and its contribution to bonding mechanism [31, 37]. Temperature rise beyond the melting point at the interface was verified in a few instances by experimental observations of splash and spheroid liquid droplets in CS of aluminium [38] and titanium [39].

A limited number of experimental studies have been reporting a correlation between particle/substrate bonding and peripheral shear zones [28, 37, 39-42] and most of these studies focused on the examination of the rebound sites at the substrate surfaces. It has been shown that a thin, Al-rich layer is left behind as a result of Al-Si particles impact onto mild steel [40]. The layer is generally ring-shaped, at the peripheral zone of the crater left in the substrate by the rebounded particle. Another study investigated the impact of titanium particles on a gold plated steel surface. The crater shape left on the substrate demonstrated that titanium particles abraded the gold surface in a ring-shape pattern near the particle edge, where the simulation predicts the highest equivalent plastic strain (PEEQ) [37]. Likewise, the morphology of detached Ti6Al4V particles and their imprint on titanium substrates revealed no bonding in the central part of the particles even for impact velocity

as high as 1000 m/s. Instead, the same ring-shape bonding area near the edges was found, in agreement with the simulation [41]. A few studies tried to show particle/substrate bonding with direct observation of the bonded area. Experimental studies of impacting titanium particles onto titanium and stainless steel substrates using focused ion beam milling (FIB), confirmed that melding of particle and substrate is most likely to occur in the peripheral zone, while cracks or microvoids were observed at the central impact zone [28, 39].

Ti–Ni based alloys are the most important practical shape memory alloys (SMA) with excellent mechanical properties [43]. It is foreseen that the CS process with the ability to develop thick and dense coatings and complex free-standing shapes [10] could be used for the production of Ni-Ti based intermetallics with CS of blended elemental precursors and subsequent heat treatment of the deposition. Cold sprayed depositions of mechanically alloyed elemental mixtures of Ni-Ti have been reported previously [9, 44] while there is no report on the cold spray behaviour of Ni/Ti and Ti/Ni dissimilar pairs.The present study aims at investigating the deformation mechanism and favourable metallurgical bonding areas of Ni/Ti and Ti/Ni pairs (particle/substrate) by using direct observation of the bonded area of single particle impacts rather than only substate craters. As-sprayed and heat-treated samples are studied and numerical simulation is used to allow further understanding of the physical mechanisms involved. Heat treatments are used to evaluate bonding areas in view of intermetallic growth in the vicinity of metallurgically bonded areas.

2. Experimental Procedure

2.1. Feedstock Powders and Substrates

Nickel powder (CP-Ni, Atlantic Equipment Engineers, Upper Saddle River, NJ, USA) and titanium powder (CP-Ti Grade 1, Advanced Powder and Coatings, Boisbriand, Canada) were used as feedstock materials. The powders size distributions were measured by laser diffraction analysis (Microtrac model S3500, Montgomeryville, PA, USA) and are presented in Figs. 1(a) and (b), revealing mean particle sizes of 24.5 μm and 30.7 μm respectively. Both powders are mostly spherical and produced by a gas atomization method (Figs.1 (c) and (d)), with some satellites present in the titanium powder. The titanium and nickel powders were sprayed onto mirror polished nickel (Ni 200 (ASTM B162)) and titanium (CP Ti Grade 2 (ASTM B265)) substrates respectively. The Vickers microhardness ($HV_{0.025}$) of Ni and Ti substrates respectively were 117 and 171.

2.2. Cold Spray

The CS system used is the commercially available EP Series SST Cold Spray System (Centerline (Windsor) Ltd., Windsor, Ontario, Canada). The system comprises a 15 kW gas heater allowing a maximum gas temperature of 500°C and a maximum gas pressure of 3.8 MPa. The stainless steel de Laval nozzle used for this work has a throat diameter of 2 mm, a diverging section length of 120 mm with an exit diameter of 6.6 mm. Nitrogen (N_2) and helium (He) were used as process gases. The feedstock powders were fed using a commercially available AT-1200HP powder feeder (Thermach Inc., Appleton, WI, USA). Three sets of single impact experiments were done using the spraying parameters (pressure and temperature) of Table 1.

2.3. Particle Velocity Measurement

The in-flight particle velocities were measured using a Cold Spray Meter (CSM) (Tecnar Automation Ltd., Saint-Bruno, QC, Canada). The particles were tracked and the average and standard deviation of the in-flight particle velocities were measured.

2.4. Characterization and Heat Treatment

For bonding analysis, some single impact samples were heat treated for 1 and 5 minutes at 700 ℃ in a vacuum furnace (with vacuum level below 10^{-6} torr). In order to ensure that Ni/Ti and Ti/Ni specimens experienced exactly the same heat-treatment conditions, both Ni/Ti and Ti/Ni samples were heat-treated simultaneously in the same zone of a vacuum furnace tube. Cross-sections of as sprayed and heat-treated samples were prepared using standard metallographical procedures. Then, top view and cross-sectional microstructures of as sprayed and heat treated single impact samples were examined using a scanning electron microscope (SEM) (EVO MA-10, Carl Zeiss AG, Oberkochen, Germany) equipped with secondary (SE) and back-scattering electron (BSE) detectors as well as x-ray energy dispersive spectroscopy (EDS).

3. Numerical Modelling

To gain more insight on the single impact deformation process and bonding of Ni/Ti and Ti/Ni pairs, axisymmetric models were employed using the commercially available finite element software ABAQUS [25, 31, 32, 45-48]. The mesh size of both the substrate and the particles near the contact surface was set to be at a maximum 1/50 of the particle diameter [25]. Severe distortion of the elements as a result of high velocity impact was alleviated by

using distortion control values. The measured mean particle size of titanium (30μm) and nickel powder (25μm) were used for simulation. The particle velocity measured using the CSM for N_2-Sprayed Ti was 456±70. The particle velocity measured for Ni powder was 459±61 m/s [36]. For that reason, the particle initial velocity was set to 500 m/s in the model, for both Ni/Ti and N_2-sprayed Ti/Ni. The impact velocity of He-sprayed Ti/Ni was approximated to be 750 m/s. The general physical properties of powders and substrate materials used in the models are given in Table 2. The initial substrate and particle temperature were set to 298 K. It is likely that both will be larger than that, especially the substrate. While the substrate temperature can be measured, the particle temperature cannot be measured due to the combination of lack of emissivity and fast travel speed making measurements almost impossible. Furthermore, the particle impact temperature is not expected to be significant with the spray parameters used while the substrate temperature will have a limited effect on the mechanical properties when compared to the contribution of impact deformation process.

The hydrodynamic stress of elastic response of the impacting particles and substrates were modelled using the Mie-Grüneisen equation of state (EOS) in the linear Us-Up Hugoniot form [36]:

$$p = \frac{\rho_0 c_0^2 \eta}{(1 - s\eta)^2}\left(1 - \frac{\Gamma_0 \eta}{2}\right) + \Gamma_0 \rho_0 E_m$$

Eq.1

$$\eta = 1 - \frac{\rho_0}{\rho}$$

Eq.2

where p is the hydrodynamic stress, ρ_0 is the initial density, c_0 is the material speed of sound, s is the Hugoniot slope coefficient, Γ_0 is the Grüneisen constant, E_m is the internal energy per unit mass, and ρ is the density.

The deviatoric stress of elastic response was assumed to be linear [36]:

$$d = 2G_e\varepsilon_s$$

Eq.3

where d is the deviatoric stress, G_e is the elastic shear modulus, and ε_s is the elastic deviatoric strain. The EOS parameters of the powders and substrate materials used in the simulations are given in Table 3.

The PTW model of flow stress was used for modelling the plastic behaviour of the impacting particles and the substrates. The flow stress (σ_y) which is a function of the equivalent plastic strain (ε_p), strain rate ($\dot{\varepsilon}_p$) and temperature (T) is defined as [35, 36]:

$$\sigma_y(\varepsilon_p, \dot{\varepsilon}_p, T) = 2\left[\hat{\tau}_s + \alpha \ln\left[1 - \varphi \exp\left(-\delta - \frac{\theta\varepsilon_p}{\alpha\varphi}\right)\right]\right] G_p(T) \qquad \text{Eq.4}$$

$$\alpha = \frac{s_0 - \hat{\tau}_y}{p}, \quad \delta = \frac{\hat{\tau}_s - \hat{\tau}_y}{\alpha}, \quad \varphi = \exp(\delta) - 1 \qquad \text{Eq.5}$$

where $\hat{\tau}_s$ is a normalized work-hardening saturation stress, $\hat{\tau}_y$ is a normalized yield stress, s_0 is the value of $\hat{\tau}_s$ at zero kelvin, θ is the strain hardening rate, and p is the strain hardening constant. Likewise, G_p denotes the shear modulus which is a function of temperature and it is defined by the equation from the mechanical threshold stress (MTS) model as [36]:

$$G_p(T) = G_0 - \frac{D}{\exp(\frac{T_0}{T}) - 1} \quad \text{Eq.6}$$

where G_0 is the shear modulus at zero kelvin, D is a material constant, T_0 is a temperature material constant, and T is the node temperature. The saturation stress ($\hat{\tau}_s$) and the yield stress ($\hat{\tau}_y$) are given by [35, 36]:

$$\hat{\tau}_s = \max\left\{ s_0 - (s_0 - s_\infty)\,\mathrm{erf}\left[\kappa \hat{T} \ln\left(\frac{\gamma\dot{\xi}}{\dot{\varepsilon}_p} \right) \right], s_0 \left(\frac{\dot{\varepsilon}_p}{\gamma\dot{\xi}} \right)^{s_1} \right\} \quad \text{Eq.7}$$

$$\hat{\tau}_y = \max\left\{ y_0 - (y_0 - y_\infty)\mathrm{erf}\left[\kappa \hat{T} \ln(\frac{\gamma\dot{\xi}}{\dot{\varepsilon}_p}) \right], \min\left\{ y_1 \left(\frac{\dot{\varepsilon}_p}{\gamma\dot{\xi}} \right)^{y_2}, s_0 \left(\frac{\dot{\varepsilon}_p}{\gamma\dot{\xi}} \right)^{s_1} \right\} \right\} \quad \text{Eq.8}$$

s_∞ is the value of $\hat{\tau}_s$ close to the melt temperature, $\hat{T} = T/T_m$, T is the temperature and T_m is the melting temperature, κ is the temperature dependence constant, γ is the strain rate dependence constant, s_1 is the high strain rate exponent, y_0 is the yield stress constant at zero kelvin, y_∞ is yield stress constant close the melting point, y_1 is the medium strain rate

constant, and y_2 is the medium strain rate exponent. The two definitions in the maximum functions are used to model both low and high strain rate regimes, respectively. The first definition of the maximum functions are used for lower strain rates at which flow stresses of deformation are governed by thermal activation mode of dislocation motion, whereas the second defenition which is used for higher strain rates where dislocation drag mechanism is governed. The material parameter $\dot{\xi}$ in Eq. 7 and Eq. 8 is defined as:

$$\dot{\xi} = \frac{1}{2}\left(\frac{4\pi\rho}{3M}\right)^{1/3}\left(\frac{G_p(T)}{\rho}\right)^{1/2}$$

Eq.9

Where ρ are the density and M represents atomic mass. The PTW material parameters for the powders and the substrates including saturation stress, yield stress, strain (rate) hardening constant and coefficient are given in Table 4. It is worth noting that the PTW model and the MTS shear behaviour are not included in ABAQUS. Consequently, these models were integrated into the finite element analysis by a user subroutine (VUHARD) [35, 36].

4. Results and Discussion

4.1. As Sprayed and Heat-Treated Single Impact Particles

Fig. 2 shows top and cross-section views from single impact particle tests for the Ni/Ti particle/substrate pair. Figs. 2 (a-c) show three different impact morphologies. Figs.2 (a and d) presents the most common impact morphology found for nickel particles. This splat

reveals some areas where the jetting phenomena is observed at the particle periphery and slight flattening of the nickel particle while the splat of Fig. 2(c) is extensively flattened. The splat of Fig. 2 (b) seems to have thick material flowing on its left side and shows lower flatting ratio compared to the two other morphologies encountered. The appearance of the top of the particle and the position of material flow (which took place somewhere far from interface area) suggest that this splat was formed as a result of collision with another particle. Craters on the substrate resulting from bounced off particles are seen in Figs. 2(a-c). The cross-section images of Figs. 2 (d-f) reveal that nickel particles deformed and flattened with shallow penetration into the titanium substrate. Particle deformation varied substantially from particle to particle potentially due to impact velocities. Limited deformation of substrate underneath well deformed and flattened particle as presented in Figs. 2 (c) and (f) suggests that impact with the nozzle wall and with other particles prior to hitting the substrate might have played an important role in the particles deformation [49].

Figure 3 shows the typical single impact morphology observed for the Ti/Ni couple. Figs. 3(a) and (d) respectively present top views of N_2 and He-sprayed Ti/Ni pair respectively. These images indicate that jetting occurs in both cases although more limited and localized for N_2-sprayed particles due to the lower impact velocities when using nitrogen [50]. Splat cross-sections (Figs.3(b) and (e)) show that the increase of particle impact velocity also results in increased particle flattening and deeper particle penetration with the presence of substrate jetting. Close-up views (Figs. 3(c) and (f)) reveal spots with different contrasts in the nickel substrate underneath the titanium splats. These are likely caused by different electron channelling conditions and indicate deformed and distorted areas caused by slight

misorientations of regions inside the deformed grains. These areas might be induced by lattice distortion through the introduction of dislocations into the substrate microstructure and potentially describe qualitatively the plastic strain field. It can be observed that the propagation of plastic zone in the nickel substrate underneath a titanium splat is limited to a few micron deep.

To investigate metallurgically bonded areas of the single impacting particles, the test samples were heat treated at 700°C for 1 minute with the hypothesis that metallurgically bonded areas will be the first locations of intermetallics nucleation and growth [15, 16]. Once intermetallic phases nucleate they will grow in vertical and lateral directions [51]. Consequently, intermetallics locally formed may coalesce and a continuous intermetallic layer will form even in areas where the bonding is imperfect.

The cross-sections of the heat-treated nickel splats and both N_2 and He–sprayed titanium splats are presented in Fig. 4. Ni-Ti intermetallic phases are identified as the regions of mid-grey contrast between the substrates and the particles. These zones were marked with dotted lines just above them for clarity. The nickel splat of Fig. 4(a) showed a different impact morphology (comparing with splats of Fig. 2) in terms of particle depth of penetration, which suggests that this particle deposited in a crater previously created by a particle that bounced off. This assumption is evaluated and potentially confirmed in section 4.2.2. A continuous layer of intermetallic phases covers the peripheral areas of the splat of Fig.4 (a) with intermetallics being absent at the centre of the splat. Fig.4 (b) shows another heat-treated nickel splat, with impact morphology similar to most commonly observed

impact morphologies of nickel splats. Intermetallics cover almost the whole interface of the nickel splat of Fig.4 (b).

The impact morphologies of N_2-sprayed Ti splats shown in Figs. 4 (c-d) and He-sprayed Ti splats in Figs. 4 (e-f), indicate that the smaller particles of each pair exhibit more deformation and higher flattening ratio. This is because of the potentially higher impact velocities of the smaller particles. Titanium splat of Fig. 4(e) shows an impact morphology similar to the one of Fig. 4 (c) while the titanium splat of Fig. 4(f) shows sharper and more pronounced jetting area, revealing a much larger impact velocity. Besides, the impact morphologies of N_2 and He-sprayed Ti splats show that He as a process gas provides a broader range of impact velocities [52].

More interfacial intermetallics have formed at the interface areas of smaller particles for both N_2- and He-sprayed Ti/Ni pairs. Cross sections of heat treated splats of N_2-sprayed titanium (Figs. 4(c-d)) and He-sprayed titanium (Figs. 4(e-f)) present the same general features of intermetallics growth. Intermetallic layers grew at the peripheral interface areas of all titanium splats while it is absent at the centre of the interface, except the smaller particle of Fig.4(d). In that case, it seems to be continuous over the entire interface surface with small holes present at the central interfacial area. Clearly, the particle cannot be cut exactly in the middle. Therefore, the cross-sectional images possibly do not show the base of the particle. Nevertheless, this discrepancy in the growth pattern can possibly be addressed both through higher impact velocity of smaller particles and through the smaller surface of these particles. The higher impact velocities of smaller particles could extend the bonding areas from peripheral shear zones towards the central areas of the interfaces.

Furthermore, the intermetallics formed in peripheral areas of smaller particles might coalesce and form continuous intermetallics layer even on the non-bonded interfaces. Additionally, small discontinuities are seen in the central interfaces between particles base and substrates which is more evident in the case of the He-sprayed titanium splat of Fig. 4(f) (marked with an arrow) which means there is no bonding at the central interface area. Nickel splats and He-sprayed titanium splats have a higher fraction of interface areas covered with intermetallic compounds in comparison with N_2-sprayed titanium splats, despite the same particle impact velocity for N_2 sprayed nickel and N_2 sprayed titanium. This can be explained by relatively more deformability of Ni particles (with FCC crystal structure) compared to titanium particles (with HCP crystal structure) for the same impact velocity and higher impact velocities of He-sprayed Ti particles, both promoting better bonding. One can also notice that the distorted plastic area is more pronounced at the nickel substrates underneath of the splats where intermetallic compounds formed.

4.2. Impact Simulations

While mechanical bonding of CS particles relies on substrate/particle topography and may reach high values depending on the level of intricacy resulting from the substrate surface treatment prior to spraying, metallic bonding relies amongst other things on the removal of the native oxide films present at the surface of the impacting particles and substrates. Removal of the oxide layer is directly related to the deformation and jetting occurring as a result of ASI [53, 54]. In order to complement the single particle impact observations made and enhance insight of the occurrence of ASI of the Ni/Ti and Ti/Ni pairs, flow stress and

temporal evolution of temperature in the sheared zone of the different pairs have been examined through modelling.

Equivalent plastic strain (PEEQ) [25, 26, 36, 47] distribution and temperature distribution [31, 32] have been used by several authors as a measure of metallurgical bonding [25, 26, 36, 47] with the assumption that the metallurgical bonding is likely to take place at the highly strained interfacial areas with high PEEQ and temperature values. This assumption will be evaluated by correlation of experimental evidence of bonding from interfacial intermetallic growth and highly strained areas predicted by FEM modelling. Additionally, as mentioned in sections 4.1 the impact of single titanium splats (Figs. 3 and 4) caused plastic deformation of nickel substrates that appeared as spots with different contrasts inside of the grains. To be able to find out about the plastic strain field underneath of the titanium splats the plastic shear strain (PE12) component will be analysed.

4.2.1. Particle/Substrate Deformation and ASI

The monitored elements of the particles and substrates that are used for outputs are marked in the geometric model of Fig. 5(a). These elements were selected as they are the elements experiencing the highest temperature increase. Only those elements were selected for the sake of concision, but other elements in their vicinity presented similar features. Thermomechanical analyses for Ni/Ti and N_2-sprayed Ti/Ni at the impact velocity of 500 m/s and He-sprayed Ti/Ni at the impact velocity of 750 m/s are provided in Figs. 5(b-d). Thermal histories of the monitored elements of all three pairs show a sudden increase of temperature, as reported previously , took place almost at the same time for both Ni/Ti and

Ti/N (500 m/s) while it happens at a slightly shorter time for Ti/Ni pair (750 m/s) (Fig.5(d)).

The maximum temperatures of 998 K, 892 K and 1280 K, are achieved respectively for Ni/Ti (500 m/s), Ti/Ni (500 m/s) and Ti/Ni (750m/s) pairs in the titanium (Figs.5(b-d). These maximum temperatures are well below Ni and Ti melting temperatures. Consequently, melting phenomenon is not expected to contribute to interfacial particle/substrate bonding of Ni/Ti and Ti/Ni pairs.

This temperature increase was accompanied by the decrease of flow stresses (for both particles and substrates). The temperature rise along with the decreasing flow stress trends is the indication of thermal softening dominance over strain (rate) hardening effect and is considered as an evidence of ASI initiation. The temporal evolution of PEEQ of monitored elements in Fig.6 shows that modelled Ti/Ni pairs at both impact velocities indicate very close PEEQ values for the substrate and impacting particle, where the PEEQ values in Ni/Ti pair is very different for nickel particle and titanium substrate. On the other hand, at both impact velocities of titanium particles, both particle and substrate deform almost to similar extents as observed experimentally. In short, for CS of the Ni/Ti pair, the deformation dominantly takes place on the particle side with relatively small amount of deformation on the substrate side (similar to soft/hard pairs), while for CS of Ti/Ni pairs, in spite of what is usually found in hard/soft systems -- for instance, Cu/Al [16], Ti/Al [31] which are known to result in particle embedment into the substrate -- both particle/substrate deform to similar extent. Generally, for the hard/soft dissimilar pairs reported in the literature (Cu/Al [16], Ti/Al [31] and Ni/Al [55]) , the hard particles are relatively dense

which can promote higher substrate deformation while in Ti/Ni pair hard Ti particles have a lower density. This means that in addition to yield strength, stiffness and hardness [31], the density of impacting particle play an import role in the substrate deformation and particle embedment of hard/soft pairs.

4.2.2. Impact Morphology: Simulation vs Experiments

Impact morphology of real nickel splats showed that most of the impacting nickel particles have shallow penetration into the titanium substrate. However, the nickel splats of Figs. 2(e) and 4(a) appeared to have deeper penetration which lead to the assumption that these particles deposited in an existing crater that was the result of a rebounded particle. This assumption is evaluated by modelling a nickel particle impact onto a crater with 14μm diameter and 4μm depth (which was the most common crater geometry observed in substrate cross-section images). Simulated impact morphologies of a nickel particle (25 μm) onto two different titanium substrate (one being a flat substrate and one including the initial crater) with an initial velocity of 500 m/s are shown in Figs. 7(a1-a2) and (b1-b2). Simulated impact of titanium particles (30 μm) onto nickel substrates with initial velocities of 500 and 750 m/s respectively are given in Figs. 7(c1-c2) and Figs.7(d1-d2). The modelling results are compared with the SEM images of splats experimentally obtained (the first and second columns vs. the third column of Fig. 7). The most frequently observed impact morphologies were taken to represent the impact conditions of the corresponding particle size. In the case of Ti/Ni pairs, for instance, large Ti splats with low flattening ratio were observed for both cases of spraying with He and N_2. However, this morphology was significantly more frequently observed in N_2-sprayed samples – hence taken as representing

the impact conditions of large Ti particles only for the case of spraying with N_2. The most frequently observed splat morphologies for Ti/Ni and Ni/Ti pairs – which are to be compared to the corresponding modelled splats – are presented in Fig.7 (a3) (c3) and (d3).

The PEEQ and temperature distributions are shown in the left and right half of each modelled splat respectively. Two simulated snapshots of nickel particles (Figs.7(a2) and (b2)) with the same impact velocity and diameter appear to have different flattening ratio and penetration to the substrate, depending on the presence of a pre-existing crater on the substrate. The nickel particle impacting on the flat substrate reaches higher PEEQ value and temperature throughout its deformation process which can be attributed to the higher strain rate encountered at the particle surface during the impact with the flat surface compared with the substrate including the initial crater (1.53×10^{9} s^{-1} vs. 1.39×10^{9} s^{-1}) [15].

In Ti/Ni pairs, PEEQ values and maximum temperature reached increase with the particle impact velocity. Both Ni/Ti pairs showed higher PEEQ values compared with both Ti/Ni pairs at two impact velocities. This can be explained by relatively higher density and more deformability of Ni particles which promote more deformation. Comparing the snapshots of simulated impacts of Ni/Ti (Fig.7(a1-a2) and Ti/Ni (Fig.7(c1-c2)) with similar impact velocity, it is seen that the nickel particle is more extensively deformed and flattened while the titanium particle appears to have a small amount of deformation with low flattening ratio. With the increase of impact velocity to 750 m/s, the titanium particle of Ti/Ni pair undergoes more deformation and jetting phenomenon becomes more pronounced (Figs. 7(d1-d2).

The highest PEEQ values in Ni/Ti pairs have been seen on the particle side. The lower PEEQ values of substrate side of Ni/Ti pairs is consistent with the lower substrate deformation as observed from shallower penetration of Ni splats into (flat) titanium substrates (Figs. 2, 4). The PEEQ contours for the titanium splat with an impact velocity of 500 m/s and 750 m/s (Fig.7(c2) and (d2) respectively) are almost equally distributed on both the particle and (nickel) substrate side.

Corresponding SEM cross-section images of each splat of Fig.7((a3)-(d3)) are in good agreement with the simulated splats in terms of overall impact morphology, flattening ratio and jetting phenomenon. In both Ni/Ti and Ti/Ni pairs the locations of grown interfacial intermetallics (marked by dotted lines at the SEM images) corresponds qualitatively well with the highly strained interface areas of the peripheries. Intermetallics formation at the highly-strained interface areas with high PEEQ values can be correlated with the possible metallurgical bonding of the as-sprayed condition and the deformation-enhanced interdiffusion phenomena. The highly strained areas are most likely to succeed to have direct metal-metal bonding [15, 16, 56] which will decrease the interdiffusion distance. Furthermore, a high level of microstructural defects such as dislocations are expected to generate and pile up at highly-strained areas which can be involved in the interdiffusion enhancement [57-61]. For instance, for the nickel substrate underneath of titanium splats (Figs. 3,4,7), the high level of defects manifests as distorted areas where the interfacial intermetallics are more likely seen in the vicinity of this region. It has been shown that the high strain rate dynamic deformation enhances interdiffusion during plastic deformation proportional to the deformation rate [62]. This confirms that highly strained interface areas

are more likely to result in clean surfaces (free of oxides) and establish metallurgical bonding where interfacial intermetallics forms at the initial steps of heat treatment.

The PE12 (plastic shear strain component) distribution of the simulated Ti splat of Fig. 7(d2) and the SEM image of He-sprayed Ti splat of Fig. 7(d3) are presented in the left and right half of Fig. 8 to allow a direct enhanced comparison. As mentioned before the distorted areas underneath of Ti splats are located mostly at the peripheral areas and PE12 component showed its maximum value at the particle peripheries. Considering this similarity between the PE12 distribution and impact induced layer combined with the distorted appearance of this layer tend to support the notion that these distorted areas mostly originated from shear strains. The distorted area appears to be related to the shear strain distribution in such a way that highly strained areas of the substrate near the interface show uniform deformation while locations away from the interface presenting a decrease or absence of shear strain present reduced or limited distortion.

4.3. Correlation of Single Splat Bonding with Peripheral Shear Zone

Fig. 9 presents further experimental pieces of evidence of particle/substrate bonding including a rebound site of a titanium particle, a fracture surface of two bonded titanium particles that presumably debonded following rebound (from a coating build-up) and interfacial intermetallic growth of a titanium single splat. SEM micrograph (half SE-half BSE) of a rebound site top view on the nickel substrate (upon impact of titanium particle) is given in Fig.9(a). Looking at the SE image (with dark grey contrast in the lower half), the depth of the penetration and substrate deformation are observed. The crater appears to be smooth at the central part surrounded by the rough surface at the rim of the crater. This

rough surface presents titanium remnants confirmed by BSE imaging (upper half), corresponding to bonded areas prior to particle bouncing off as a result of elastic energy. This image points out that the limited bonded area at the rim of the crater failed to overcome rebounding forces and the particle bounced off.

The fracture surface of two bonded titanium particles (Fig.9(b)) presents details of interparticle bonding. The bonded areas are evident with dimple fractures occurring at the peripheries far from the central smooth area. The fracture morphology of bonded area in Fig.9(b) confirms that ring-shaped bonding pattern took place in the peripheral shear zone of impacting particle similar to those reported in Refs [37, 40, 41]. Providing direct evidence of bonding at the peripheries, this imprint reveals the localized nature of ASI which leads to non-uniform and discontinuous bonding pattern.

The cross-section of a heat treated single particle splat of He-sprayed Ti/Ni pair is shown in Fig.9(c). This sample was heat treated at 700℃ for a longer time than previous samples (5 min vs. 1 min heat treatment of previous samples). Jetting of the particle and the substrate (marked in Fig.9 (c)) is observed and gaps can be seen at the substrate jetting areas (both sides) and at the base of the titanium particle. Comparing this heat-treated splat with the heat-treated splats of Fig.4, it is observed that a significant part of this titanium splat transformed into intermetallic components (interfacial intermetallics thickness ≈ 0.5 μm vs. 5.5 μm). EDS analysis of the intermetallic layers revealed Ti_2Ni and Ni_3Ti formed at the titanium-rich and nickel-rich areas respectively with NiTi phases formed in between, as reported elsewhere [63]. Being the thickest layer of the intermetallic compounds, NiTi phase grew twice as thick as the others meaning that its growth rate was dominant over the

growth rate of the two other intermetallics. In spite of two other intermetallics, the Ni_3Ti phase did not grow uniformly and it failed to form in the substrate jetting areas while being thin at the base of the splat. The intermetallic components formed at the interface of the titanium splat/nickel substrate and grew toward the titanium particles while the growth of intermetallics in the nickel substrate is negligible. Studies on the intermetallic growth mechanism of Ni/Ti couple have shown that Ni_3Ti and Ti_2Ni form respectively at the nickel side and titanium side of the interface at initial steps of phase formation while NiTi phase is the product of secondary reactions [64, 65]. Additionally, it has been shown that the interfacial intermetallics are more likely to nucleate and grow from highly strained peripheral areas. Putting all these points together, one can conclude that the Ni_3Ti/Ni interface is almost located at the original splat/substrate interface. Then, it can be stated that Ni_3Ti phase mostly formed at metallurgically bonded areas which means that initial bonding state of the particle/substrate influence the phase formation kinetics.

Comparing the bonding evidence from rough surface and titanium remnant of the crater of Fig.9(a), dimple fracture surfaces of metallurgically bonded areas of Fig.9(b), the intermetallic growth pattern of Figs.4(c-d) and 9(c), and PEEQ distribution of simulated snapshots of Fig.7, one can conclude that most of the metallurgically bonded spots of the interface are located in the peripheral zones. Furthermore, improving spraying condition like increase of impact velocity (associated with using of He compared to N_2 gas or small splats which are potentially impacted with higher velocities) and impact of relatively high mass density and more deformable Ni particle (in same spraying condition) bonding area extends from rims of the particle to the base of the particle.

6. Conclusion

Experiments were performed to study the bonding phenomena in the cold spraying of Ni/Ti and Ti/Ni pairs. Impact morphology of single splats was modelled through FEM simulations. The PTW plasticity model was used for modelling of the large strain rates experienced during the cold spray process. Particle/substrate bonding can be characterised with respect to the growth of an intermetallic phase at the interface after heat treatment.

1. It was found that for the Ni/Ti pair, plastic deformation of the Ni particle is dominating whereas for the Ti/Ni pairs at both impact velocities both substrates and particles deformed to similar extents.
2. Single impact studies showed that distorted areas formed at nickel substrates underneath of the peripheral shear zones following the impact of titanium particles onto the nickel substrate. The distribution of this distorted area correlates with the distribution of shear strain component of PE12 in the single impact modellings.
3. From the simulation and interfacial intermetallics growth results, it is found that metal-metal bonding is likely to take place in highly strained areas of particle/substrate interfaces.
4. It has been shown that initial bonding condition of a single splat could influence the kinetic of intermetallics growth.
5. The fast intermetallic growth kinetics of heat-treated single impact and the onset of intermetallics formation from peripheral areas is attributed to deformation-enhanced interdiffusion.

6. The experimental evidence of bonding in combination with single impact simulations demonstrated that the bonding areas extend from peripheries toward the central part of the interfaces with increasing kinetic energy of impact.

Acknowledgements

A part of this work was performed during a research visit of R. Nikbakht at Cold Spray laboratory of University of Ottawa and she is grateful to University of Ottawa for support throughout the research visit. The authors would like to thank D. Macdonald (University of Ottawa, Canada) for assistance with the velocity analysis experiments. Also, authors thank S. Rahmati (University of Ottawa, Canada) for allowing them to use the user subroutine (VUHARD) of PTW model. R.Nikbakht appriciates having helpful conversations with Prof. M. Yandouzi (University of Ottawa, Canada).

References

[1] H. Assadi, H. Kreye, F. Gärtner, T. Klassen, Cold spraying–a materials perspective, Acta Mater. 116 (2016) 382-407.

[2] P. Cavaliere, A. Perrone, A. Silvello, Cold-Sprayed Nanostructured Pure Cobalt Coatings, J. Therm. Spray Technol. 25 (2016) 1168-1176.

[3] M.R. Rokni, C.A. Widener, A.T. Nardi, V.K. Champagne, Nano crystalline high energy milled 5083 Al powder deposited using cold spray, Appl. Surf. Sci. 305 (2014) 797-804.

[4] R. Ghelichi, D. MacDonald, S. Bagherifard, H. Jahed, M. Guagliano, B. Jodoin, Microstructure and fatigue behavior of cold spray coated Al5052, Acta Mater. 60 (2012) 6555-6561.

[5] P. Richer, A. Zúñiga, M. Yandouzi, B. Jodoin, CoNiCrAlY microstructural changes induced during Cold Gas Dynamic Spraying, Surf. Coat. Technol. 203 (2008) 364-371.

[6] D. Goldbaum, J.M. Shockley, R. Chromik, A. Rezaeian, S. Yue, J.-G. Legoux, E. Irissou, The Effect of Deposition Conditions on Adhesion Strength of Ti and Ti6Al4V Cold Spray Splats, J. Therm. Spray Technol. 21 (2012) 288-303.

[7] W.Y. Li, C. Zhang, X.P. Guo, G. Zhang, H.L. Liao, C. Coddet, Deposition characteristics of Al–12Si alloy coating fabricated by cold spraying with relatively large powder particles, Appl. Surf. Sci. 253 (2007) 7124-7130.

[8] S.W. Dean, J.K. Potter, R.A. Yetter, T.J. Eden, V. Champagne, M. Trexler, Energetic intermetallic materials formed by cold spray, Intermetallics 43 (2013) 121-130.

[9] Y. Zhou, C.-J. Li, G.-J. Yang, H.-D. Wang, G. Li, Effect of self-propagating high-temperature combustion synthesis on the deposition of NiTi coating by cold spraying using mechanical alloying Ni/Ti powder, Intermetallics 18 (2010) 2154-2158.

[10] T. Novoselova, S. Celotto, R. Morgan, P. Fox, W. O'neill, Formation of TiAl intermetallics by heat treatment of cold-sprayed precursor deposits, J. Alloys Compd. 436 (2007) 69-77.

[11] A. Bacciochini, M. Radulescu, Y. Charron-Tousignant, J. Van Dyke, M. Nganbe, M. Yandouzi, J. Lee, B. Jodoin, Enhanced reactivity of mechanically-activated nano-scale gasless reactive materials consolidated by coldspray, Surf. Coat. Technol. 206 (2012) 4343-4348.

[12] A. Moridi, S. Hassani-Gangaraj, M. Guagliano, M. Dao, Cold spray coating: review of material systems and future perspectives, Surf. Eng. 30 (2014) 369-395.

[13] R. Gonzalez, H. Ashrafizadeh, A. Lopera, P. Mertiny, A. McDonald, A Review of Thermal Spray Metallization of Polymer-Based Structures, J. Therm. Spray Technol. 25 (2016) 897-919.

[14] M. Robotti, S. Dosta, C. Fernández-Rodríguez, M.J. Hernández-Rodríguez, I.G. Cano, E.P. Melián, J.M. Guilemany, Photocatalytic abatement of NOx by C-TiO2/polymer composite coatings obtained by low pressure cold gas spraying, Appl. Surf. Sci. 362 (2016) 274-280.

[15] A. Nastic, M. Vijay, A. Tieu, S. Rahmati, B. Jodoin, Experimental and Numerical Study of the Influence of Substrate Surface Preparation on Adhesion Mechanisms of Aluminum Cold Spray Coatings on 300M Steel Substrates, J. Therm. Spray Technol. 26 (2017) 1461–1483.

[16] T. Hussain, D.G. McCartney, P.H. Shipway, Bonding between aluminium and copper in cold spraying: story of asymmetry, Mater. Sci. Technol. 28 (2013) 1371-1378.

[17] H. Bu, M. Yandouzi, C. Lu, B. Jodoin, Effect of heat treatment on the intermetallic layer of cold sprayed aluminum coatings on magnesium alloy, Surf. Coat. Technol. 205 (2011) 4665-4671.

[18] D. MacDonald, R. Fernández, F. Delloro, B. Jodoin, Cold Spraying of Armstrong Process Titanium Powder for Additive Manufacturing, J. Therm. Spray Technol. 26 (2016) 598–609.

[19] G. Bae, K. Kang, J.-J. Kim, C. Lee, Nanostructure formation and its effects on the mechanical properties of kinetic sprayed titanium coating, Mater. Sci. Eng., A 527 (2010) 6313-6319.

[20] J. Liu, X. Zhou, X. Zheng, H. Cui, J. Zhang, Tribological behavior of cold-sprayed nanocrystalline and conventional copper coatings, Appl. Surf. Sci. 258 (2012) 7490-7496.

[21] X. Suo, X. Guo, W. Li, M.-P. Planche, R. Bolot, H. Liao, C. Coddet, Preparation and characterization of magnesium coating deposited by cold spraying, J. Mater. Process. Technol. 212 (2012) 100-105.

[22] P. Richer, B. Jodoin, L. Ajdelsztajn, Substrate roughness and thickness effects on cold spray nanocrystalline Al−Mg coatings, J. Therm. Spray Technol. 15 (2006) 246-254.

[23] T. Schmidt, F. Gärtner, H. Assadi, H. Kreye, Development of a generalized parameter window for cold spray deposition, Acta Mater. 54 (2006) 729-742.

[24] M. Grujicic, J.R. Saylor, D.E. Beasley, W. DeRosset, D. Helfritch, Computational analysis of the interfacial bonding between feed-powder particles and the substrate in the cold-gas dynamic-spray process, Appl. Surf. Sci. 219 (2003) 211-227.

[25] H. Assadi, F. Gärtner, T. Stoltenhoff, H. Kreye, Bonding mechanism in cold gas spraying, Acta Mater. 51 (2003) 4379-4394.

[26] M. Grujicic, C.L. Zhao, W.S. DeRosset, D. Helfritch, Adiabatic shear instability based mechanism for particles/substrate bonding in the cold-gas dynamic-spray process, Mater. Des. 25 (2004) 681-688.

[27] K. Kim, M. Watanabe, S. Kuroda, Thermal softening effect on the deposition efficiency and microstructure of warm sprayed metallic powder, Scripta Mater. 60 (2009) 710-713.

[28] K. Kim, M. Watanabe, K. Mitsuishi, K. Iakoubovskii, S. Kuroda, Impact bonding and rebounding between kinetically sprayed titanium particle and steel substrate revealed by high-resolution electron microscopy, J. Phys. D: Appl. Phys. 42 (2009) 065304-065309.

[29] W.-Y. Li, H. Liao, C.-J. Li, H.-S. Bang, C. Coddet, Numerical simulation of deformation behavior of Al particles impacting on Al substrate and effect of surface oxide films on interfacial bonding in cold spraying, Appl. Surf. Sci. 253 (2007) 5084-5091.

[30] A. Vardelle, C. Moreau, J. Akedo, H. Ashrafizadeh, C.C. Berndt, J.O. Berghaus, M. Boulos, J. Brogan, A.C. Bourtsalas, A. Dolatabadi, The 2016 Thermal Spray Roadmap, J. Therm. Spray Technol. (2016) 1-65.

[31] G. Bae, Y. Xiong, S. Kumar, K. Kang, C. Lee, General aspects of interface bonding in kinetic sprayed coatings, Acta Mater. 56 (2008) 4858-4868.

[32] S. Dosta, G. Bolelli, A. Candeli, L. Lusvarghi, I.G. Cano, J.M. Guilemany, Plastic deformation phenomena during cold spray impact of WC-Co particles onto metal substrates, Acta Mater. 124 (2017) 173-181.

[33] T. Schmidt, H. Assadi, F. Gärtner, H. Richter, T. Stoltenhoff, H. Kreye, T. Klassen, From Particle Acceleration to Impact and Bonding in Cold Spraying, J. Therm. Spray Technol. 18 (2009) 794.

[34] W.-Y. Li, S. Yin, X.-F. Wang, Numerical investigations of the effect of oblique impact on particle deformation in cold spraying by the SPH method, Appl. Surf. Sci. 256 (2010) 3725-3734.

[35] S. Rahmati, A. Ghaei, The Use of Particle/Substrate Material Models in Simulation of Cold-Gas Dynamic-Spray Process, J. Therm. Spray Technol. 23 (2013) 530-540.

[36] Y. Cormier, P. Dupuis, B. Jodoin, A. Ghaei, Finite Element Analysis and Failure Mode Characterization of Pyramidal Fin Arrays Produced by Masked Cold Gas Dynamic Spray, J. Therm. Spray Technol. 24 (2015) 1549-1565.

[37] K. Kim, M. Watanabe, S. Kuroda, Jetting-Out Phenomenon Associated with Bonding of Warm-Sprayed Titanium Particles onto Steel Substrate, J. Therm. Spray Technol. 18 (2009) 490-499.

[38] P. King, M. Yandouzi, B. Jodoin, The Physics of Cold Spray, in: J. Villafuerte (Ed.), Modern Cold Spray: Materials, Process, and Applications., Springer International Publishing, Cham, 2015, pp. 31-72.

[39] P.C. King, C. Busch, T. Kittel-Sherri, M. Jahedi, S. Gulizia, Interface melding in cold spray titanium particle impact, Surf. Coat. Technol. 239 (2014) 191-199.

[40] J. Wu, H. Fang, H. Kim, C. Lee, High speed impact behaviors of Al alloy particle onto mild steel substrate during kinetic deposition, Mater. Sci. Eng., A 417 (2006) 114-119.

[41] M.V. Vidaller, A. List, F. Gaertner, T. Klassen, S. Dosta, J.M. Guilemany, Single Impact Bonding of Cold Sprayed Ti-6Al-4V Powders on Different Substrates, J. Therm. Spray Technol. 24 (2015) 644-658.

[42] Q.S. Lin, K.S. Zhou, C.M. Deng, M. Liu, X.L. Xiao, C.G. Deng, Deposition behavior and microstructural development of TiNi powder particles in low temperature-HVOF spraying process, Appl. Surf. Sci. 283 (2013) 352-359.

[43] K. Otsuka, X. Ren, Physical metallurgy of Ti–Ni-based shape memory alloys, Prog. Mater Sci. 50 (2005) 511-678.

[44] S. Tria, O. Elkedim, R. Hamzaoui, X. Guo, F. Bernard, N. Millot, O. Rapaud, Deposition and characterization of cold sprayed nanocrystalline NiTi, Powder Technol. 210 (2011) 181-188.

[45] Y. Xie, S. Yin, C. Chen, M.-P. Planche, H. Liao, R. Lupoi, New insights into the coating/substrate interfacial bonding mechanism in cold spray, Scripta Mater. 125 (2016) 1-4.

[46] J. Henao, A. Concustell, S. Dosta, G. Bolelli, I.G. Cano, L. Lusvarghi, J.M. Guilemany, Deposition mechanisms of metallic glass particles by Cold Gas Spraying, Acta Mater. 125 (2017) 327-339.

[47] Z. Arabgol, M. Villa Vidaller, H. Assadi, F. Gärtner, T. Klassen, Influence of thermal properties and temperature of substrate on the quality of cold-sprayed deposits, Acta Mater. 127 (2017) 287-301.

[48] G. Bae, K. Kang, H. Na, J.-J. Kim, C. Lee, Effect of particle size on the microstructure and properties of kinetic sprayed nickel coatings, Surf. Coat. Technol. 204 (2010) 3326-3335.

[49] D. MacDonald, S. Leblanc-Robert, R. Fernández, A. Farjam, B. Jodoin, Effect of Nozzle Material on Downstream Lateral Injection Cold Spray Performance, J. Therm. Spray Technol. 25 (2016) 1149-1157.

[50] T. Van Steenkiste, 8 - The role of particle temperature and velocity in cold spray coating formation A2 in: V.K. Champagne (Ed.), The Cold Spray Materials Deposition Process: fundamentals and applications, Woodhead Publishing, New York, 2007, pp. 127-147.

[51] C.J. Hang, C.Q. Wang, M. Mayer, Y.H. Tian, Y. Zhou, H.H. Wang, Growth behavior of Cu/Al intermetallic compounds and cracks in copper ball bonds during isothermal aging, Microelectron. Reliab. 48 (2008) 416-424.

[52] W. Wong, E. Irissou, A.N. Ryabinin, J.-G. Legoux, S. Yue, Influence of Helium and Nitrogen Gases on the Properties of Cold Gas Dynamic Sprayed Pure Titanium Coatings, J. Therm. Spray Technol. 20 (2011) 213-226.

[53] Y. Xie, M.-P. Planche, R. Raoelison, P. Hervé, X. Suo, P. He, H. Liao, Investigation on the influence of particle preheating temperature on bonding of cold-sprayed nickel coatings, Surf. Coat. Technol. 318 (2016) 99-105.

[54] F. Meng, D. Hu, Y. Gao, S. Yue, J. Song, Cold-spray bonding mechanisms and deposition efficiency prediction for particle/substrate with distinct deformability, Mater. Des. 109 (2016) 503-510.

[55] S. Kumar, G. Bae, C. Lee, Influence of substrate roughness on bonding mechanism in cold spray, Surf. Coat. Technol. 304 (2016) 592-605.

[56] T.S. Price, P.H. Shipway, D.G. McCartney, E. Calla, D. Zhang, A Method for Characterizing the Degree of Inter-particle Bond Formation in Cold Sprayed Coatings, J. Therm. Spray Technol. 16 (2007) 566-570.

[57] B. Khina, I. Solpan, G. Lovshenko, Modelling accelerated solid-state diffusion under the action of intensive plastic deformation, J Mater Sci 39 (2004) 5135-5138.

[58] S. Pabi, D. Das, T. Mahapatra, I. Manna, Mathematical modelling of the mechanical alloying kinetics, Acta Mater. 46 (1998) 3501-3510.

[59] X.-T. Luo, C.-X. Li, F.-L. Shang, G.-J. Yang, Y.-Y. Wang, C.-J. Li, High velocity impact induced microstructure evolution during deposition of cold spray coatings: A review, Surf. Coat. Technol. 254 (2014) 11-20.

[60] A.L. Ruoff, Enhanced diffusion during plastic deformation by mechanical diffusion, J. Appl. Phys. 38 (1967) 3999-4003.

[61] X.L. Wu, N.R. Tao, Q.M. Wei, P. Jiang, J. Lu, K. Lu, Microstructural evolution and formation of nanocrystalline intermetallic compound during surface mechanical attrition treatment of cobalt, Acta Mater. 55 (2007) 5768-5779.

[62] D. Wolf, S. Yip, Materials interfaces: atomic-level structure and properties, Springer Science & Business Media, London, 1992.

[63] G.F. Bastin, G.D. Rieck, Diffusion in the titanium-nickel system: I. occurrence and growth of the various intermetallic compounds, Metall. Trans. 5 (1974) 1817-1826.

[64] X. Shao, X. Guo, Y. Han, Z. Lin, J. Qin, W. Lu, D. Zhang, Preparation of TiNi films by diffusion technology and the study of the formation sequence of the intermetallics in Ti–Ni systems, J. Mater. Res. 29 (2014) 2707-2716.

[65] A. Fuji, Y. Horiuchi, K. Yamamoto, Friction welding of pure titanium and pure nickel, Sci. Technol. Weld. Joining 10 (2005) 287-294.

Table 1. Process conditions used in CS of single impact Ni/Ti and Ti/Ni.

Single impact samples	Substrate material	Feedstock powder	Inlet Gas	Temperature (℃)	Pressure (Mpa)	Standoff distance (mm)	Traverse speed (mm/s)
Ni/Ti	CP-Ti G2	CP-Ni	N_2	500	3.4	15	25
N_2-Ti/Ni	Ni-200	CP-Ti G1	N_2	500	3.4	15	25
He-Ti/Ni	Ni-200	CP-Ti G1	He	500	3.2	15	25

Table 2. General properties of the materials used in the simulations.

Parameter	Symbol	Cp-Ti	Cp-Ni
Shear modulus GPa	G	40	76
Gruüneisen's constant	Γ_0	1.23	1.83
Speed of sound, m/s	C_0	5020	4542
Hugoniot slope	s	1.536	1.5

Table 3. Elastic and EOS parameters used in the simulations

Parameter	unit	Symbol	Cp-Ti	Cp-Ni
Density	kg/m^3	ρ	4510	8890
Melting point	K	T_m	1943	1726
Conductivity	W/(m K)	k	21.9	91
Specific heat	J/(kg K)	Cp	530	456

Table 4. PTW parameters used in the simulations [36].

Parameter	Symbol	Cp-Ti G1	Cp-Ti G2	Cp-Ni
Saturation stress at T=0 K	s_0	0.007	0.01	0.0045
Saturation stress at melting	s_∞	0.0012	0.0012	0.00055
Yield stress Constant at 0 K	y_0	0.0015	0.0015	0.0001
Yield stress Constant at Melting	y_∞	0.0005	0.0005	0.0001
Strain hardening constant	p	1.4	1.4	2
Temperature dependence constant	k	0.14	0.14	0.11
Strain rate dependence constant	γ	1.00E-05	1.00E-05	1.00E-05
Strain hardening rate	θ	0.04	0.04	0.01
Atomic mass, kg/atom	M	7.95E-26	7.95E-26	9.24E-26
High Strain rate exponent	s_1	0.25	0.25	0.25
Medium strain rate constant	y_1	0.007	0.007	0.094
Medium strain rate exponent	y_2	0.25	0.25	0.575
Shear modulus at 0 K, Gpa	G_0	48	48	85
Material constant, GPa	D	7.5	7.5	9.13
Temperature material constant, K	T_0	269	269	269

Figure Captions

Figure 1. Measured particle distribution of nickel and titanium feedstock powders (a and b), and SEM micrographs of nickel and titanium feedstock powders (c and d).

Figure 2. Morphology of Ni particles after impact on a Ti substrate (500°C, 3.4 MPa, N_2): (a-c) SEM top views and (d-f) cross-sections of Ni splats. (a) and (d) represent the most common impact geometry found.

Figure 3.SEM image of top views and cross-section of Ti particles sprayed on Ni substrates. The first row (a-c) shows N_2-sprayed Ti splats (500°C, 3.4 MPa, N2) and the second row (d-f) illustrates He-sprayed Ti splats (500°C, 3.2 MPa, He).

Figure 4. Backscattered scanning electron images of heat-treated splats (700°C for 1min). (a-b) Cross-section images of Ni/Ti, (c-d) N_2-sprayed Ti/Ni, and (e-f) He-sprayed Ti/Ni. The interfacial intermetallic are marked by dotted lines just above them.

Figure 5. The position of monitored elements on the meshed axisymmetric model and temporal evolution of temperature and Von Mises flow stress at these elements. (a) Tracked elements, (b) Ni/Ti pair (500 m/s) (c)

Ti/Ni pair (500 m/s) and (d) Ti/Ni (750 m/s). Temperature and flow stress of particle for all three pairs are shown with black lines. Temperature and flow stress of substrate for all three pairs are shown with grey lines.

Figure 5. Temporal evolution of the equivalent plastic strain (PEEQ) for monitored element shown in Fig.5(a). The PEEQ evolutions are plotted with solid and dashed lines respectively for particles and substrates. The black, light grey and grey colors respectively shows PEEQ evolution of Ni/Ti (500 m/s), Ti/Ni (500m/s) and Ti/Ni (750m/s).

Figure 6. Results of particle impact simulations vs. SEM image of the corresponding single impacts. The distribution of the equivalent plastic strain (PEEQ) and temperature of each snapshot respectively shown in left and right half of splats. First row and second rows show impact morphologies of Ni/Ti pairs at which 25 μm Ni particle impacted respectively onto a flat substrate and a substrate including the initial crater with the initial velocity of 500 m/s. Third and fourth rows show impact morphologies of Ti/Ni pairs at which 30 μm Ti particle impacted onto Ni substrates respectively with the initial impact velocities of 500 and 750 m/s.

Figure 7. Impact morphology and distribution of the shear plastic strain (PE12) of simulated Ti splat (30 μm) with the impact velocity of 750 m/s and the SEM image of He-sprayed Ti respectively in left and right half of the splat.

Figure 8. (a) Rebound site of an impacting titanium particle on nickel substrate (upper half BSE and the lower half SE), (b) fracture surface of two bonded Ti particles (from a coating build-up) (c) heat treated He-sprayed titanium splat for 5 min at 700℃.

Figure

Click here to download high resolution image

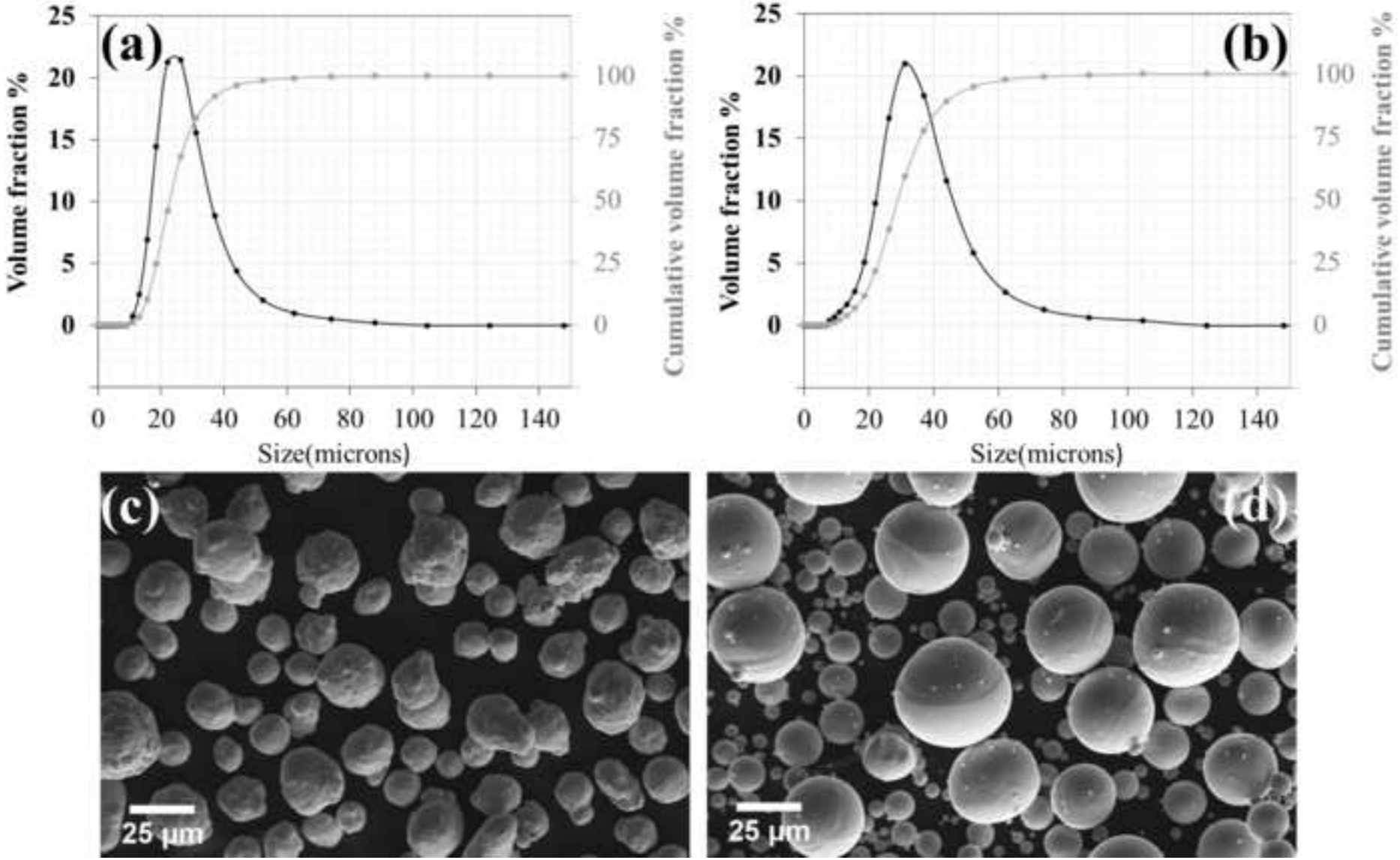

Figure
Click here to download high resolution image

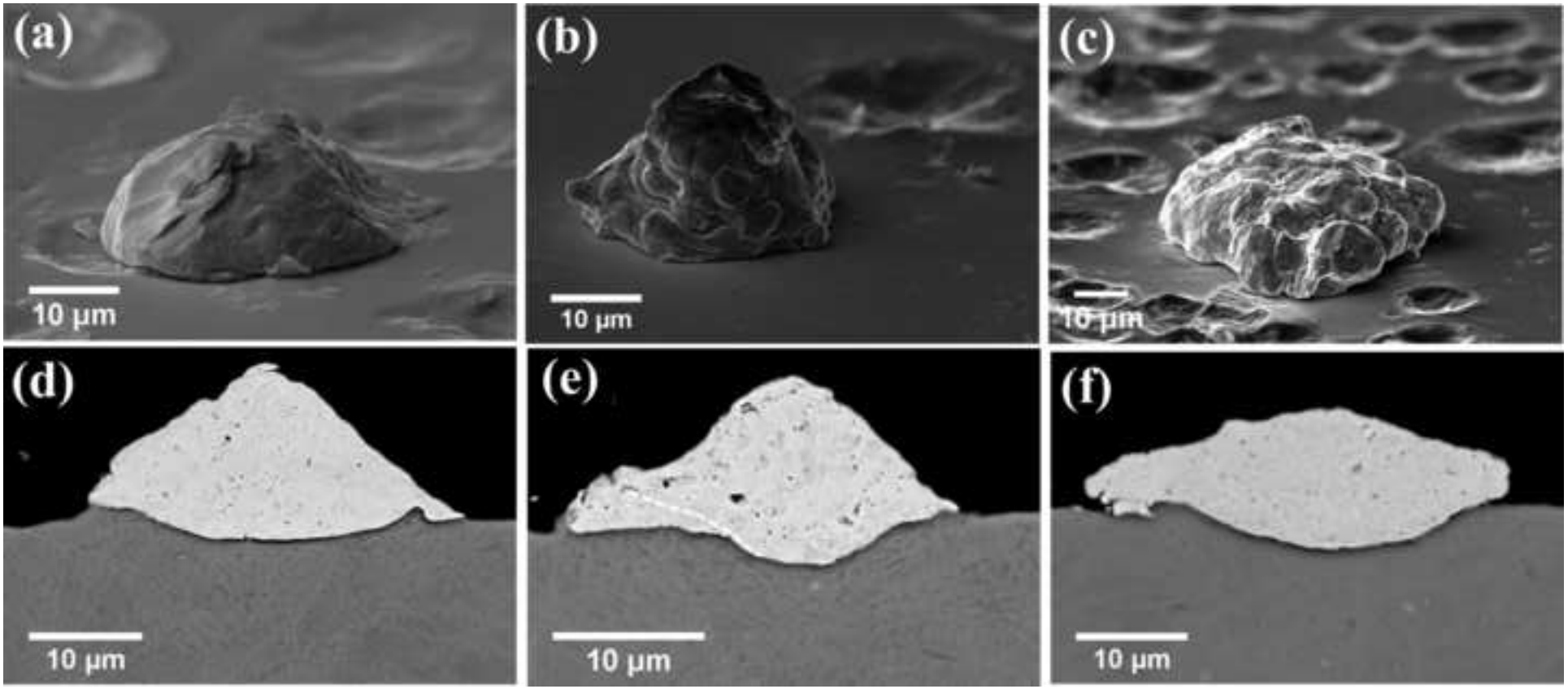

Figure
Click here to download high resolution image

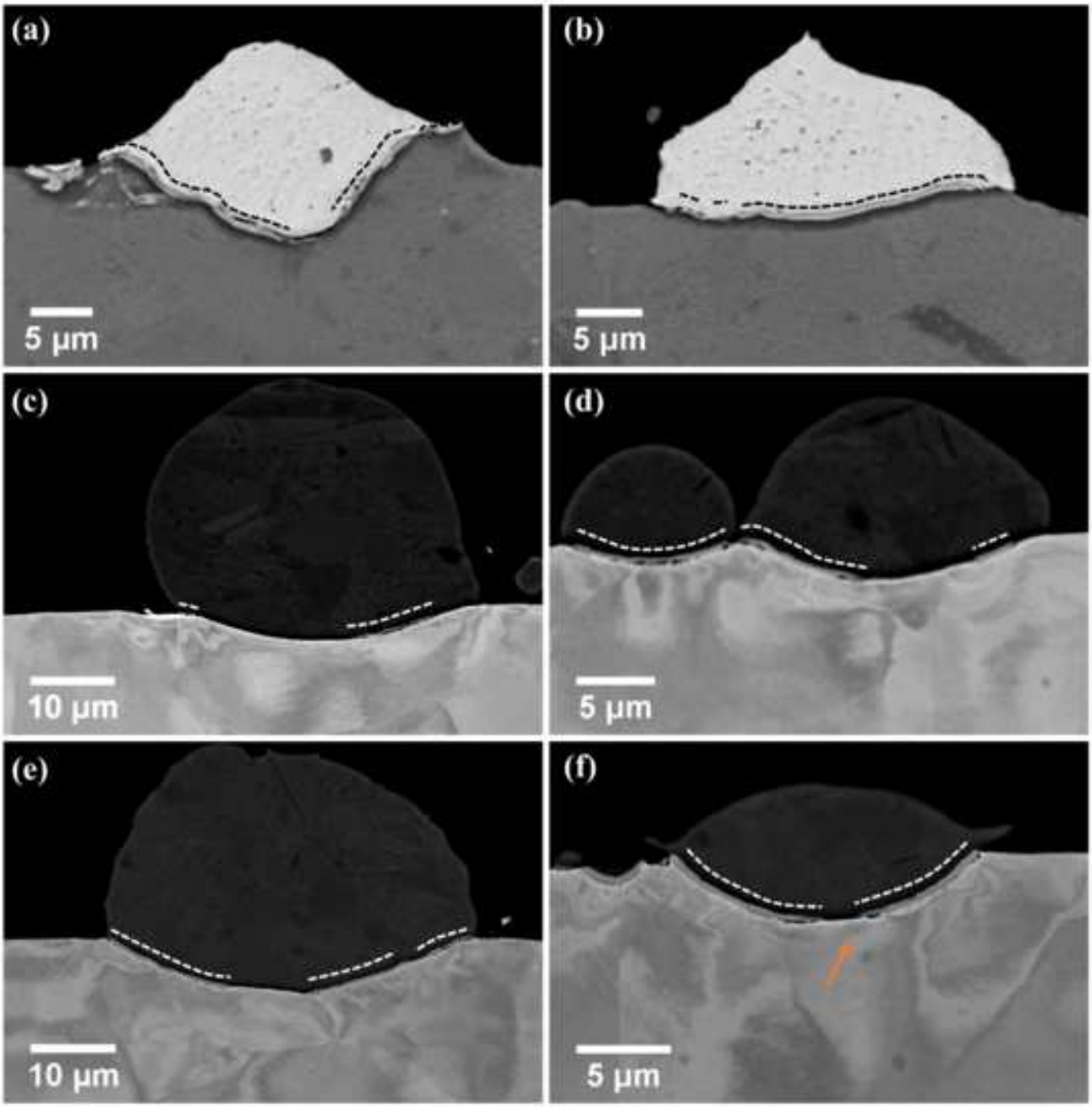

Figure

Click here to download high resolution image

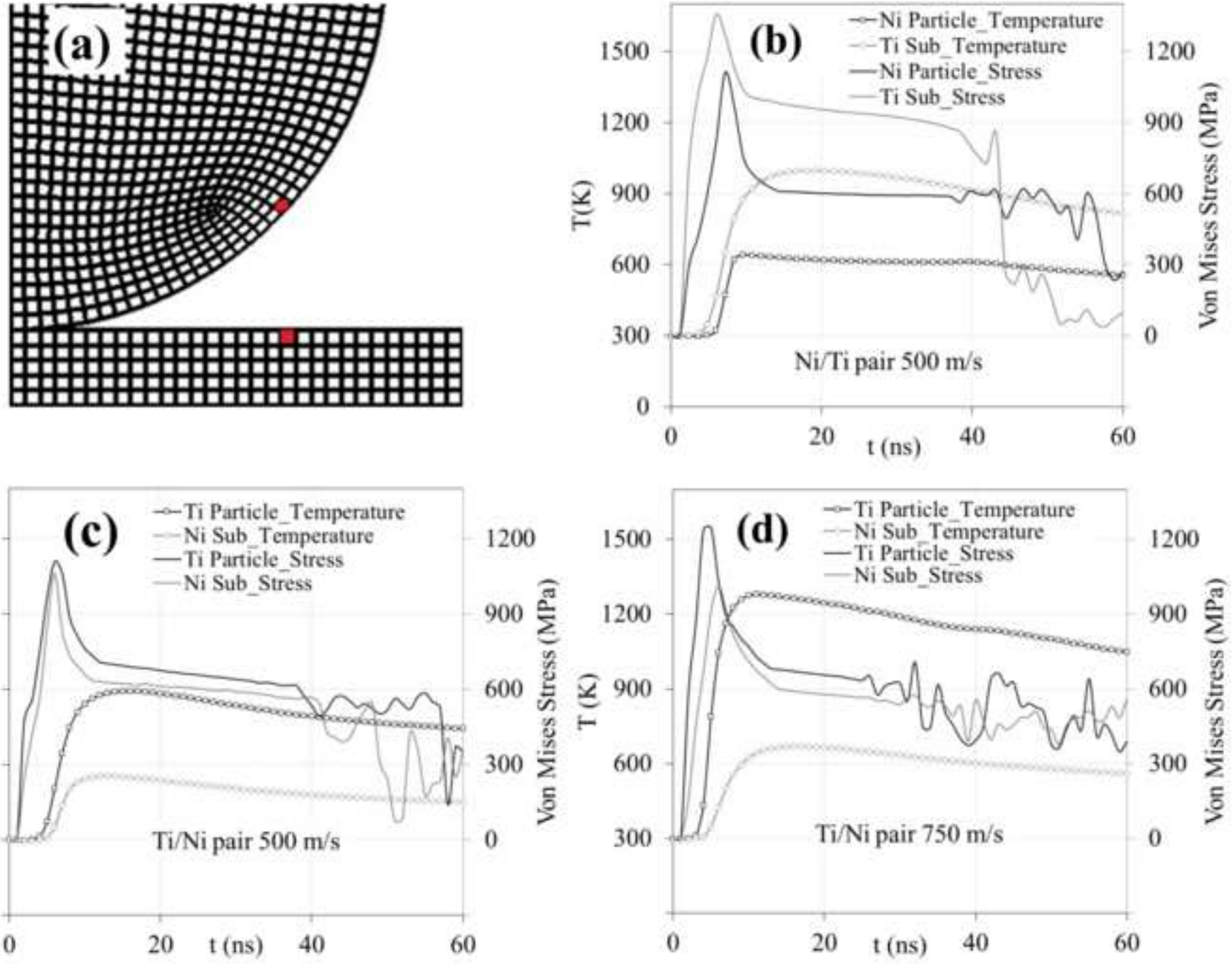

Figure

Click here to download high resolution image

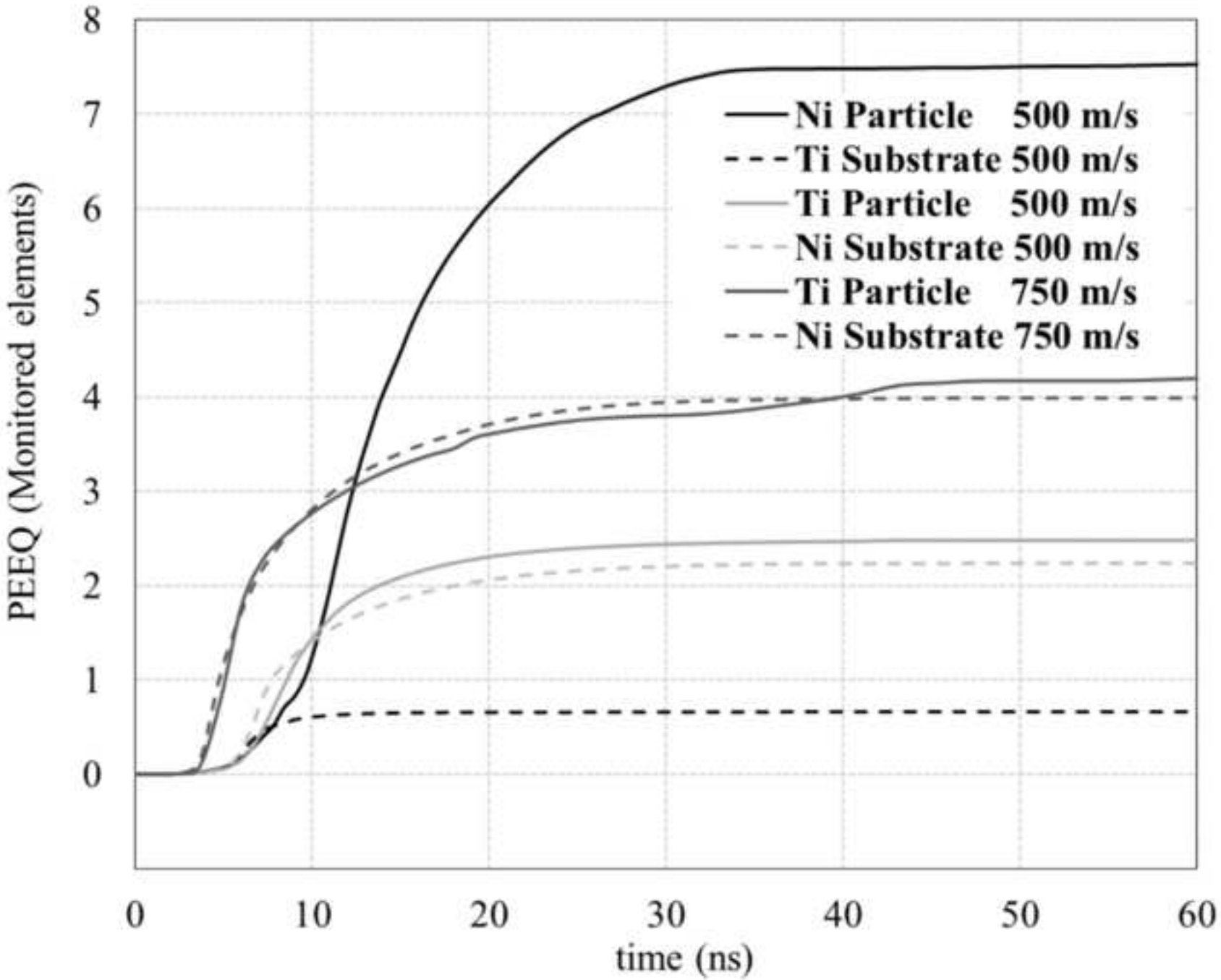

Figure

Click here to download high resolution image

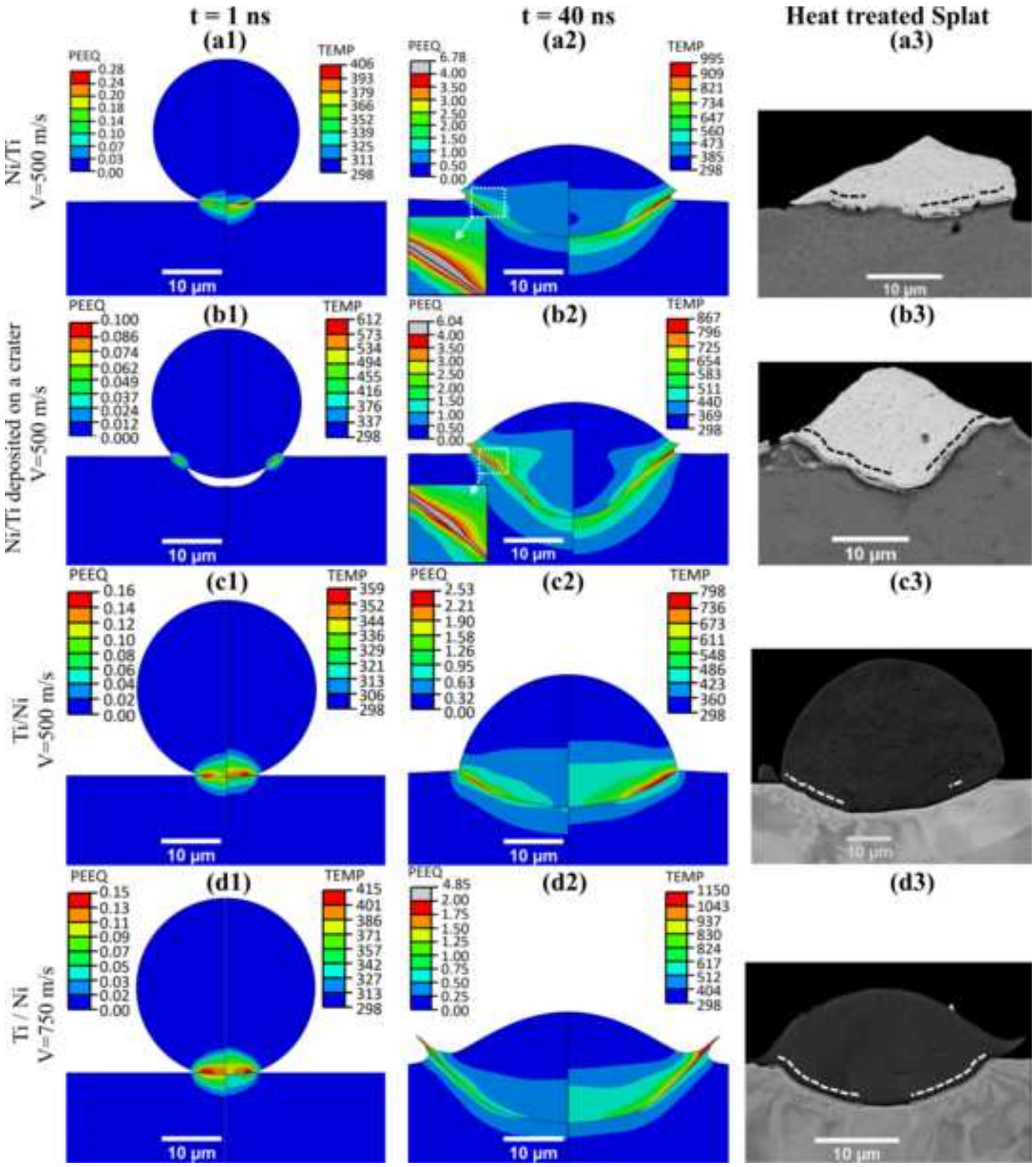

Figure
Click here to download high resolution image

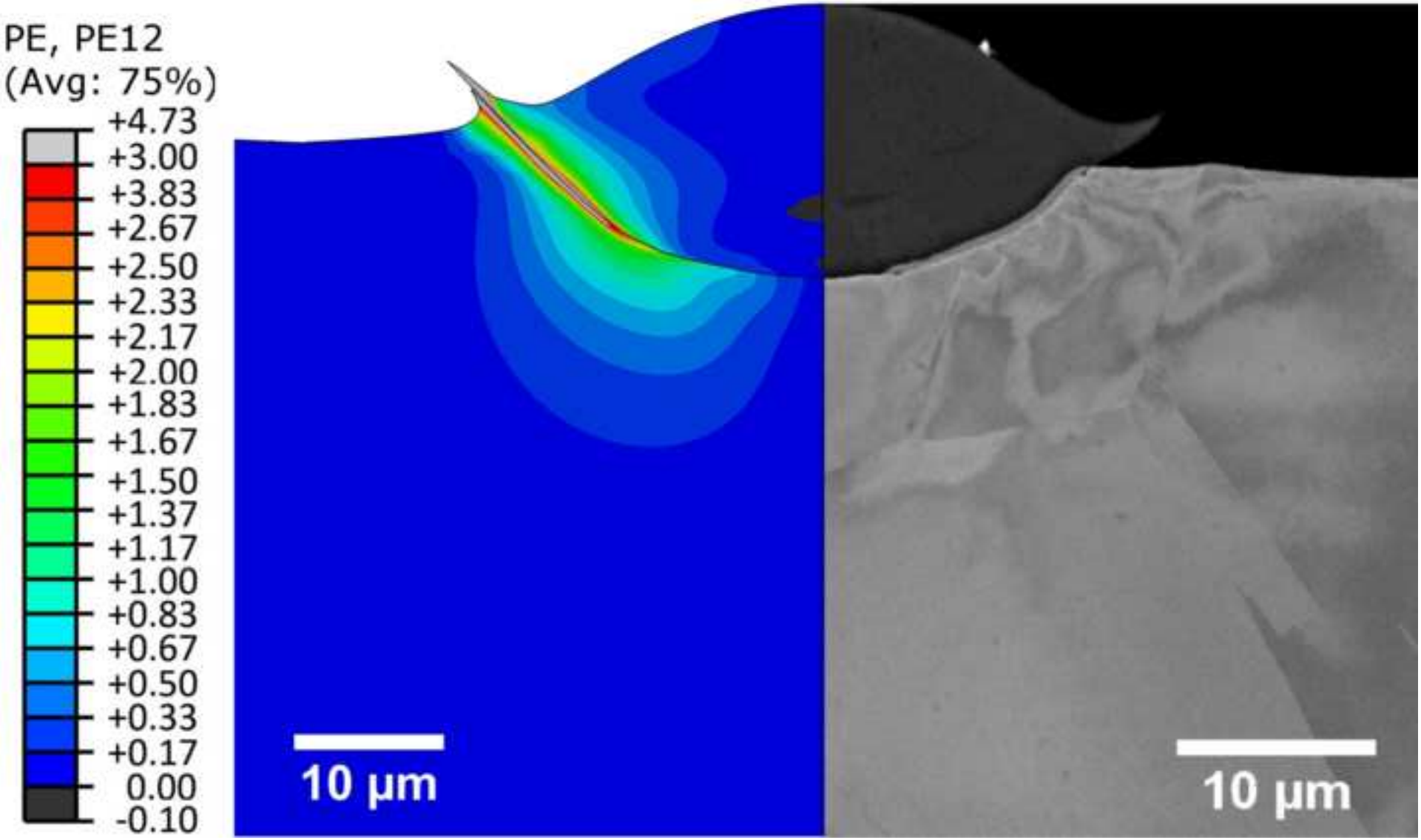

Figure
Click here to download high resolution image

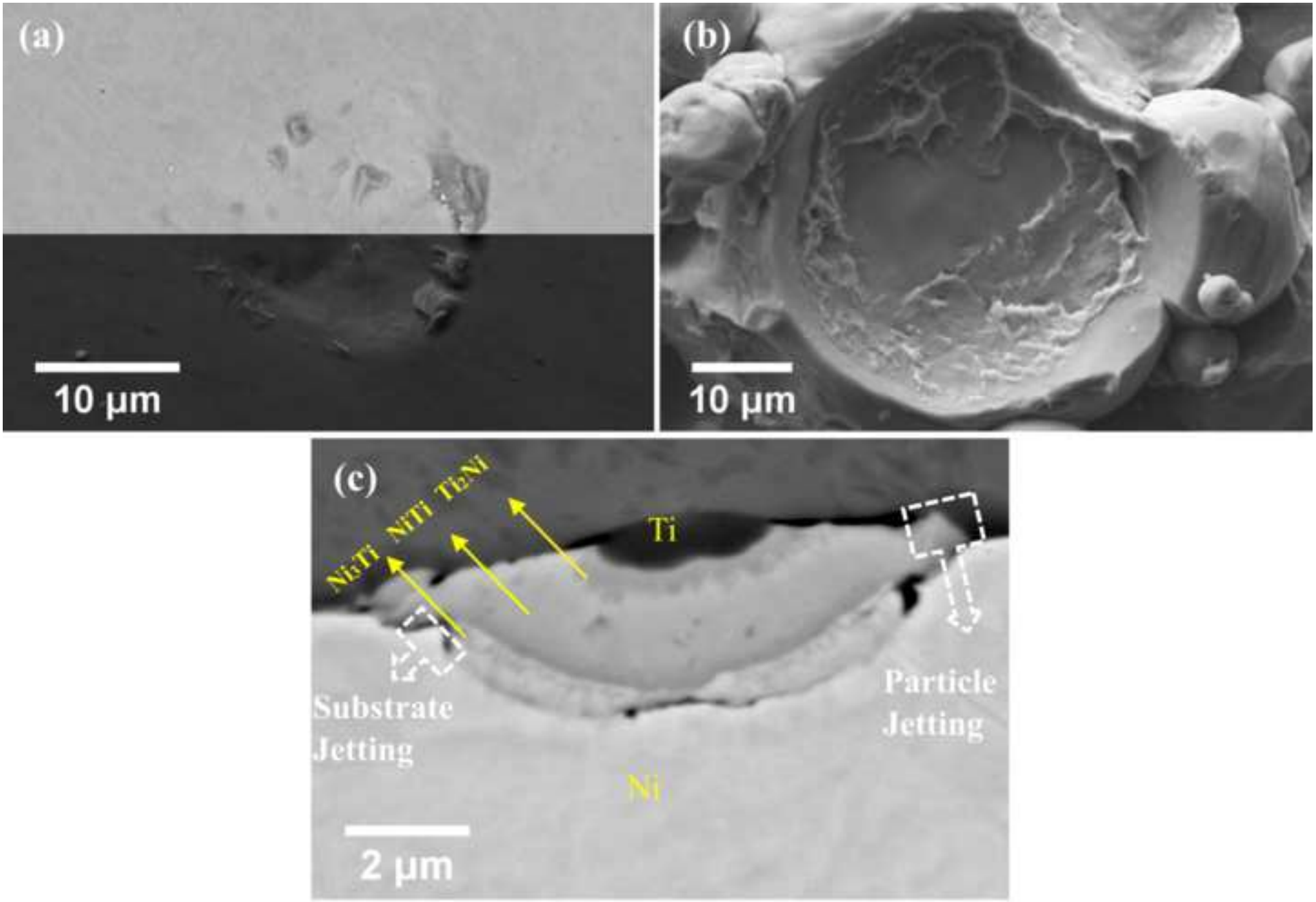

Figure
Click here to download high resolution image